Die Grenzen der Chemie neu ausloten? It takes #HumanChemistry

Wir suchen kreative Chemikerinnen und Chemiker, die mit uns gemeinsam neue Wege gehen wollen – mit Fachwissen, Unternehmertum und Kreativität für innovative Lösungen. Informieren Sie sich unter:

evonik.de/karriere

EVONIK
Leading Beyond Chemistry

Synthetic Biofuels by Molten-Salt Catalytic Conversion: Corrosion of Structural Materials in Ternary Molten Chlorides

Alexander Bonk,* Andrea Hanke, Markus Braun, Wenjin Ding, and Thomas Bauer

The molten-salt catalytic conversion of biomass into synthetic fuels is one of the promising renewable energy topics of the 21st century. Mixtures of Zn–Na–K//Cl have gained attention, acting as catalytically active heat transfer fluids in the conversion process, due to their low costs and principally low melting points which effectively lower the required operating temperature in the catalytic reactor. Herein, the corrosion behavior of three candidate steels, SS316L, SS321, and Alloy 800, in the pure molten salt, in a salt–biomass mix, and in a salt–biomass mix containing a corrosion inhibitor (zinc oxide (ZnO)) is comprehensively investigated. The herein described study demonstrates that biomass additions increase the penetration depth of the salt, and the corrosion mechanism leads to partial spalling of the oxide scale. This is attributed to the presence of oxygen and moisture from the biomass leading to the formation of reactive HCl gas. The addition of ZnO reduced the corrosivity of the molten salt–biomass mix, and all alloys obtained a protective, adherent, and thin oxide scale leading to the conclusion that ZnO indeed is an effective corrosion inhibitor for the presented salt system. These findings constitute a major advance in the implementation of molten salt-catalytic reactors for renewable synthetic fuel production.

1. Introduction

Molten salts have a wide variety of applications ranging from heat transfer fluids (HTF) to storage media for different fields of application, such as concentrating solar power (CSP),[1,2] waste heat recovery,[3] and chemical syntheses.[4] The field of molten salt-catalytic conversion has gained more interest only recently, although a few reports date back to the 1970s[5] (see also the review of Nygard et al.[6] and literature cited therein). In this thermal process, a feedstock is converted to a mixture of liquids (e.g., oils and tars), non-condensable gases (e.g., CO, CO_2, H_2, CH_4), and a few solid residues.[7–9] The most relevant fraction, the pyrolysis oils, is liquids at room temperature and exhibits around half of the heating value of fossil fuels, owing to their higher moisture and oxygen content as highlighted by Czernik and Bridgwater.[10] Nevertheless, the same authors emphasized that "using slow pyrolysis liquid did not indicate fundamental differences in combustion behavior of [...] petroleum-based fuel oils," as cited from a previous study.[10] The molten salts act as heat carriers, solvents, and catalysts simultaneously with the benefit of allowing higher heating rates than in classical thermal pyrolysis (in the air). Those higher heating rates in turn lead to higher valuable liquid fractions.[11]

Chloride salts have a high potential to be used at extremely high temperatures up to 800 °C (e.g., MgNaK//Cl mixtures), but can also be used as low-melting point HTF, such as in the case of eutectic ZnNaK//Cl ($T_m = 200$ °C).[12] Together with adequate heat capacities, chloride salts are the most promising HTF for molten salt-catalytic conversion processes. Nonetheless, technical challenges arise from their chemical nature. In the field of thermal energy storage, chloride salts have been investigated thoroughly due to their corrosive nature toward metallic alloys at high temperatures. It is generally accepted that the corrosion mechanism is affected by a number of parameters, mainly temperature, salt purity, and the presence of mainly oxygen- and/or moisture-based impurities (see, e.g., Ding's review on corrosion in molten chloride salts[12]). In $MgCl_2$-based molten salts, which play a significant role in future thermal energy storage, the main corrosive impurity has been identified as a hydroxychloride species (MgOHCl), and it is assumed to be a product from the hydrolysis of hydrated $MgCl_2$.[12,13] The impurity levels can be substantially reduced using different methods, e.g., electrolytic salt purification[14] or the addition of sacrificial agents, such as elemental Mg,[15] that react with the impurities to form inert MgO. In a similar fashion, the addition of solid oxides (e.g., ZnO and CaO) leads to a significant reduction of hydrolysis reactions of

A. Bonk, A. Hanke, M. Braun, W. Ding
German Aerospace Center (DLR)
Institute of Engineering Thermodynamics
70569 Stuttgart, Germany
E-mail: alexander.bonk@dlr.de

T. Bauer
German Aerospace Center (DLR)
Institute of Engineering Thermodynamics
51147 Cologne, Germany

The ORCID identification number(s) for the author(s) of this article can be found under https://doi.org/10.1002/adem.202101453.

**ADVANCED
SCIENCE NEWS**
www.advancedsciencenews.com

**ADVANCED
ENGINEERING
MATERIALS**
www.aem-journal.com

the respective chloride salts, $ZnCl_2$ and $CaCl_2$.[16,17] This is attributed to the fact that the oxides are able to react with HCl formed during hydrolysis and react back to the respective chlorides according to

$$MO + 2HCl \rightarrow MCl_2 + H_2O \qquad (1)$$

where M is the metal cation (e.g., Zn or Ca). By adding inhibiting metal oxides to a molten salt, the molten salt's corrosivity can be reduced, thereby prolonging the lifetime of the reactor system.

Corrosion data of alloys in molten chloride salts have been reviewed over a wide temperature range and a variety of salt compositions.[12] Generally, corrosion is very selective toward active alloying elements, e.g., those with the lowest reduction potential, such as chromium.[13,18–20] Grégoire and coworkers[21] identified that reactive impurities can selectively attack chromium carbides contained in the grain boundaries of Inconel 600 leading to continuous dissolution–precipitation reactions and eventually the formation of galvanic pairs. Furthermore, the formation of $MgCr_2O_4$ spinels, which has also been observed in other studies, derived from synergistic dissolution during acidic fluxing of MgO and basic fluxing of Cr_2O_3.

Zinc chloride is one of the most common impurities in incineration plants and can lead to excessive corrosion of boilers. Corrosion of alloys in contact with $ZnCl_2$ has been assessed in a variety of studies with a broad range of molten salt mixtures.[22–26] The corrosion mechanism depends on numerous factors, and the implications made for the case of Zn-impurities in incineration plants do not necessarily hold true for other chloride-based molten salts. As an example, Sánchez Pastén and Spiegel reported that corrosion of samples covered with a PbKZn//Cl salt exacerbated with the presence of molybdenum in the alloy, while the presence of Si and Al increased the corrosion resistance.[26] Ishitsuka and coworkers found the opposite when studying Na,K//Cl-based molten chlorides, where additions of Mo and Si to the alloy improve its corrosion resistance.[27] While in the case of Sánchez Pastén and Spiegel's example, low melting alloys between Pb, Zn, and Mo may be responsible for the enhanced corrosion, the mechanism changes in a Na,K// Cl-based molten salt. Corrosion in these salts is driven by the basicity of the melt, which is explained at length in Ishitsuka's article.[27] In summary, basicity, defined as the activity of an oxide ion (O^{2-}), is mainly affected by partial pressures of water and HCl. The basicity of the melt determines the stability of metal oxides, especially that of the oxide layers formed during a corrosion process. Layers of Cr_2O_3 are unstable at low oxygen partial pressures (leading to CrO_4^{2-} formation), while they are stable in a salt with high basicity. Ishitsuka proposes that metal oxides, such as MoO_x, which can be formed on the alloy surface

during corrosion, increase the basicity of the melt and thereby decrease the solubility of Cr_2O_3.

At the time of writing, the number of studies performed in the ternary ZnNaK//Cl molten salts is limited. Vignarooban et al. published corrosion data of Hastelloy types in ZnNaK//Cl (52.9–13.4–33.7 mol%, respectively) at 500 °C showing that the C types (C-276, C-22) were more corrosion resistant than Hastelloy N.[28] In another study, the same authors evaluated the corrosion performance of Hastelloys and an SS304 alloy in the absence and presence of air between 200 and 800 °C, using the same salt type. The corrosion rates decreased significantly when operating the salt under an inert gas atmosphere, suggesting that Hastelloy C-276 can be used as container material in CSP applications at high temperatures.

The motivation of this work is to understand the fundamental corrosion behavior of some common structural materials in the promising ZnNaK//Cl molten salt. Furthermore, we intended to investigate the impact of biomass additions and also that of a potential corrosion inhibitor on the corrosion mechanisms, as observed by electron microscopy and elemental analyses. This work will allow for a preselection of steels suitable for the construction of reservoir tanks, tubes, and other system components, as well as economic analyses in the future.

2. Experimental Section

Corrosion experiments were performed using three steel candidates: 1.4404 (SS 316L), 1.4541 (SS 321), and 1.4876 (Alloy 800) with nominal compositions presented in **Table 1**.

Sample coupons with approximate dimensions of $20 \times 10 \times 3$ mm were polished with P600 SiC paper, washed with isopropyl alcohol, and dried before being placed in nine crucibles made of high-purity alumina (one sample per crucible). The specimens were topped with 50 g of molten ZnNaK//Cl salt (Zn–Na–K: 44.3–13.8–41.9 mol%), which was prepared in a glovebox by stoichiometric weighing of KCl, NaCl (both ≥99%, Merck KGaA Darmstadt), and $ZnCl_2$ (98%, E. Merck Darmstadt). Crucibles were sealed with a flange that contains inlets for gases, thermocouples, and sample extraction. The setup used in the present research has been described in a previous study in more detail.[29] A purge gas of pure N_2 (5.0 grade) was used for each crucible (flow rate 100 mL min^{-1}). For those experiments performed in "salt + biomass" (**Table 2**), 0.5 g lignin was added to the crucibles. For the experiments designated "salt + biomass + ZnO" (**Table 2**), 0.5 g lignin and 5 g ZnO (produced from thermal decomposition of $ZnCO_3$ (Zinc Carbonate AC, RU00712105, Brüggemann Chemical, Heilbronn) at 500 °C for 2 h) were added on top of the salt. The crucibles were placed in a furnace and

Table 1. Atomic composition of the selected alloys.

Alloy	Fe	Cr	Ni	Mo	Mn	Si	Ti	C	Cu	Al
1.4404 (316L)	Bal.	16.5–18.5	10–13	2–2.5	Max. 2.0	Max. 1.0	–	Max. 0.03	–	–
1.4541 (321)	Bal.	17–19	9–12	–	Max. 2.0	Max. 1.0	Max. 0.7	Max. 0.08	–	–
1.4876 (Alloy 800)	Bal.	19–21.5	30–32	–	0.5–1.0	0.2–0.6	0.2–0.5	Max. 0.1	Max. 0.5	0.2–0.4

Table 2. Alloy samples and experimental conditions of the corrosion tests. See experimental details in the textual corpus of this section.

Sample No.	Alloy	Salt mixture	Exposure temperature [°C]	Exposure duration [h]
1	1.4404 (316L)		400 °C	800 h
2	1.4541 (321)	Salt		
3	1.4876 (Alloy 800)			
4	1.4404 (316L)			
5	1.4541 (321)	Salt + biomass		
6	1.4876 (Alloy 800)			
7	1.4404 (316L)			
8	1.4541 (321)	Salt + biomass + ZnO		
9	1.4876 (Alloy 800)			

heated to 400 °C (average salt temperature) and remained at this temperature for ≈800 h before being extracted.

Corrosion specimens were initially impregnated in epoxy resin and the cross sections were subsequently prepared water-free using petroleum oil. Due to the high solubility of $ZnCl_2$ in dehydrated acetone (used for cleansing the cross-section surfaces from petroleum oil), the salt deposits were partially dissolved, which led to strong rounding of the edges. The high solubility of zinc chloride in dehydrated acetone was unknown at that point.

To investigate the corrosion attack, samples were demounted and ultrasonically cleansed in distilled water. The samples were thereafter galvanically Ni-plated to enhance the contrast between the oxide scales and the mounting media, and the cross sections were prepared via the traditional metallographic methods involving the wet automated grinding with progressively finer SiC paper and polishing down to 1 μm using diamond solutions. Despite the dissolution of the salt deposits on the samples due to aqueous contact, it can be ensured that the oxide scales which were adherent to the metallic surface were maintained and characterized. The cross sections of 1.4404 were etched using V_2A pickle, and the cross sections of 1.4541 and 1.4876 were etched electrolytically with oxalic acid. Etched cross-sectional imaging was conducted using light optical microscopy.

Side surfaces and top surfaces of the cross sections of investigated alloys were characterized using light optical microscopy, electron probe microanalysis (EPMA, JEOL JXA-8100), and scanning electron microscopy (SEM, Philips XL-40). Unless stated otherwise, the quantitative EPMA line scans were measured from the center of the back-scattering electron (BSE) micrographs with a spatial resolution of 0.5 μm.

3. Results and Discussions

3.1. Light Microscopy Images

Light microscopy images of the Ni-plated, embedded, polished, and etched cross sections of 1.4404, 1.4541, and 1.4876 were recorded and are shown in **Figure 1**. The microstructure looks homogeneous in terms of average grain size from the top surface and side surface view. This indicates that cold rolling of the samples (during production) did not lead to elongation of grains and that the corrosion process "per se" should not be different when comparing top or side surfaces.
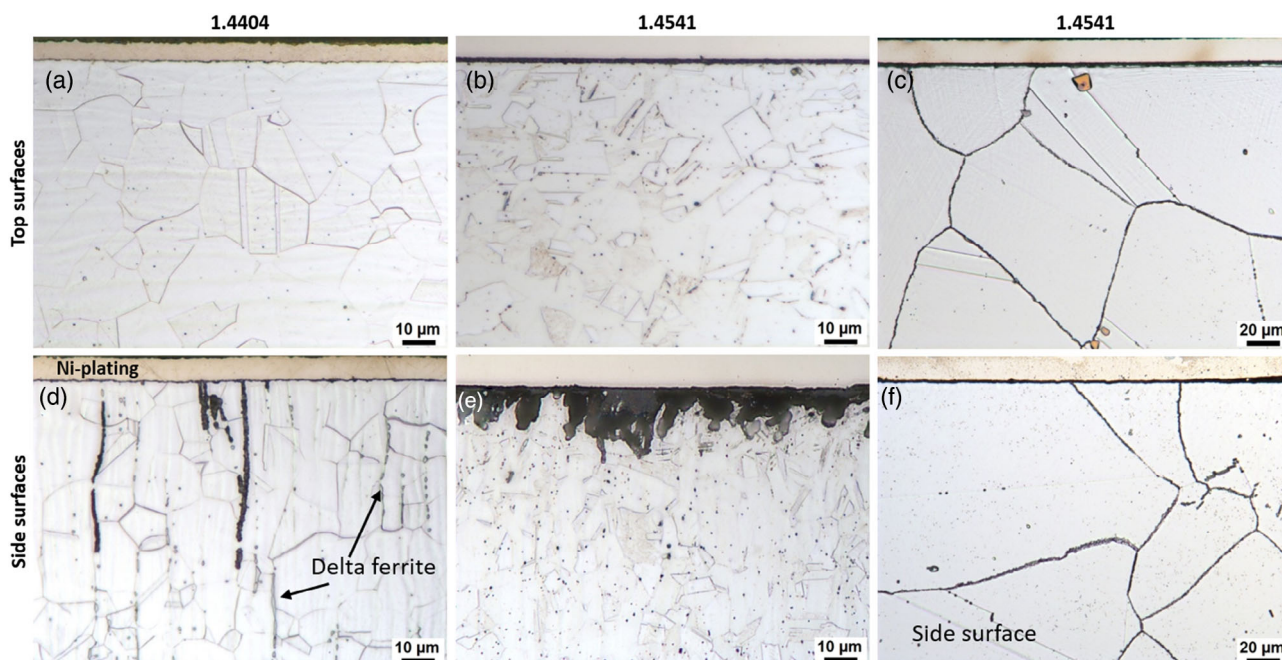

Figure 1. Light microscopy images of the polished and etched cross sections of 1.4404, 1.4541, and 1.4876 after the corrosion in salt. Images feature top surfaces in the top row and side surfaces in the bottom row. The magnification for SEM images of the 1.4876 steel is lower compared to those of 1.4404 and 1.4541, due to its larger average grain size.

ADVANCED
SCIENCE NEWS

www.advancedsciencenews.com

ADVANCED
ENGINEERING
MATERIALS

www.aem-journal.com

Looking at the polished and etched cross sections of 1.4404 (Figure 1a,d), we observed that the microstructure of the side surfaces features delta-ferrite phases along the grain boundaries, which is not the case for the top surfaces. After careful review, we assume that these phases formed during the preparation of the samples, as the metals were cut along the side surface by a cut-off machine in the DLR labs. It is possible that the surface was either not cooled enough during cutting or the feed speed was too high, leading to local heating of the sample and eventually the formation of the precipitation of delta phases. It is important to note that corrosion has been more pronounced along these delta phases, but also that delta phases are known to cause ductility loss in austenite alloys in general.[30,31] On the top surfaces, no delta-ferrite phases were observed, which indicates that it was not present in the as-received samples and only formed during sample preparation.

On the side surfaces of 1.4541 (Figure 1b,e), no delta-ferrite phases are observed, yet, they show a stronger corrosive attack than the top surfaces. Given that the bulk microstructure is otherwise very similar, we assume that these local differences in corrosion depth can be attributed to the different preparation of side and top surfaces. While top surfaces (10×20 mm) can be polished straightforwardly using automated polishing techniques, the side surfaces (3×10 mm) are prepared manually, which may lead to more inhomogeneous surface qualities.

The top and side surfaces of Alloy 800 (Figure 1c,f) are very homogeneous overall in terms of grain size, grain orientation, and preparation quality. This is reflected by very homogeneous scale thicknesses over the whole sample surface.

3.2. Corrosion in Pure ZnNaK//Cl

The cross-sectional BSE images, EPMA element maps, and line scans of 1.4404 after exposure to ZnNaK//Cl at 400 °C for 800 h are shown in **Figure 2**. The oxide scale grown is adherent and exhibits a maximum thickness of 4 μm (measured by SEM), and a lower contrast in BSE mode than the galvanically deposited Ni-layer and the bulk metal. It appears to be layered with an inner layer depleted in Cr (slightly enriched in Ni) and vice versa on the outer layer. Both layers are depleted in iron and strongly enriched with Zn and Cl, but also Na and K. It is reasonable to assume that the first layer (viewing from the bulk) is not actively enriched in Ni, but rather depleted in Cr, leading to the observed enrichment in Ni. The depletion in chromium derives from outward diffusion of Cr to form a Cr-rich layer outer oxide layer with around 20 wt% chromium and decreasing concentrations of iron toward the salt interface.

Overall, the oxide layer is very adherent and appears to be nonporous, given that no epoxy resin is infiltrating any existing pores (indicated by the low carbon signals). In the light microscopy
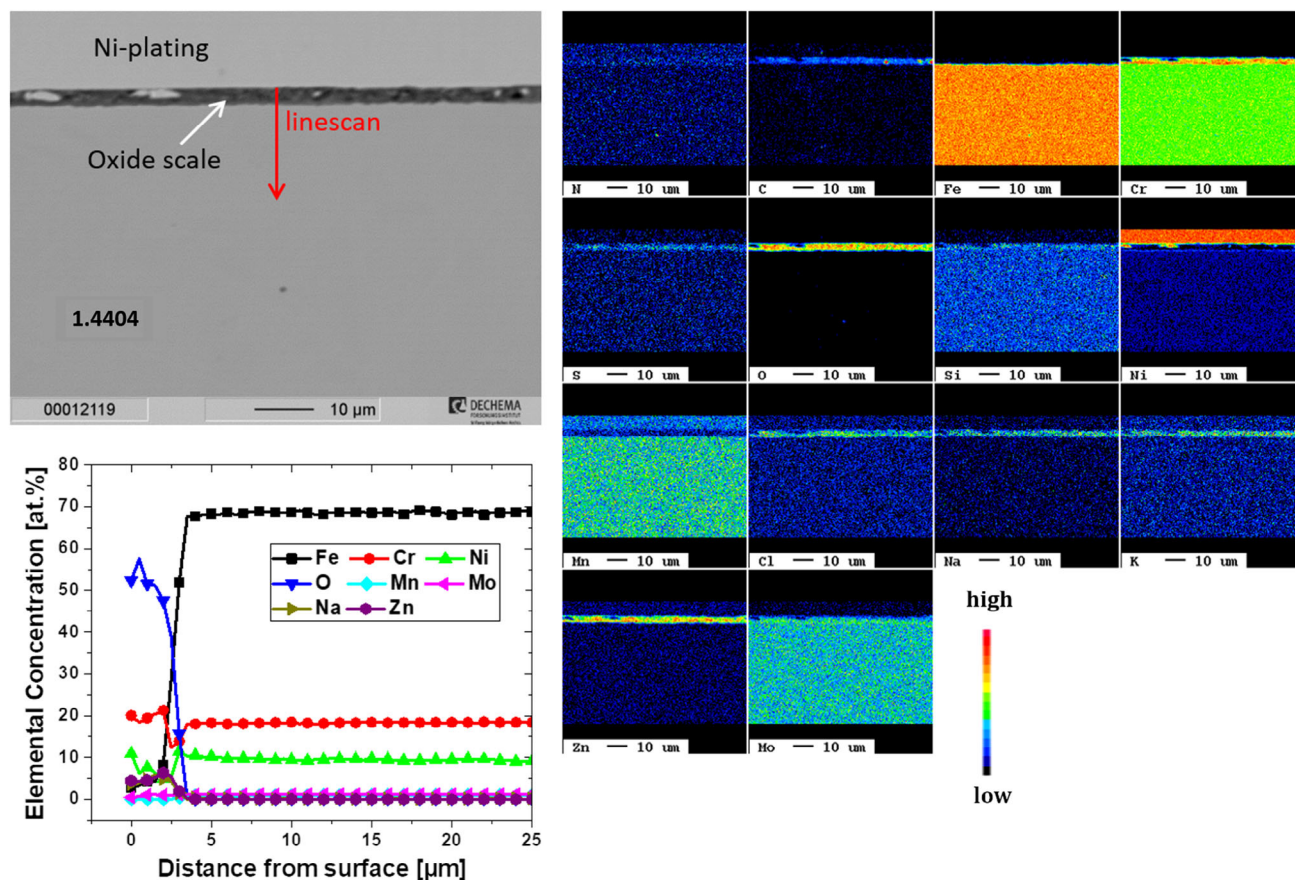

Figure 2. BSE image (top left), line scan (bottom left), and energy-dispersive X-ray spectroscopy (EDX) maps of 1.4404 exposed to pure ZnNaK//Cl for 800 h at 400 °C.
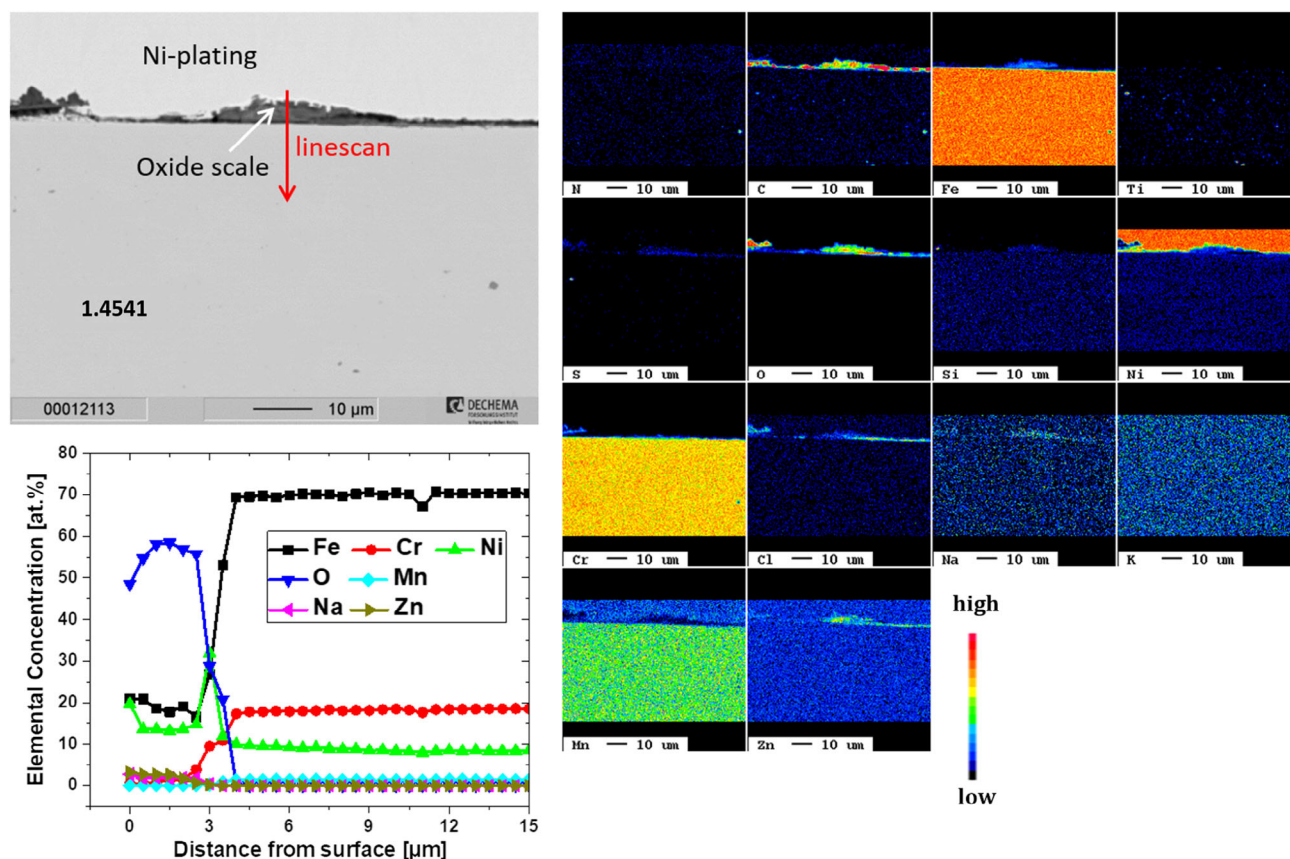
2101453 (4 of 9)

Figure 3. BSE image (top left), line scan (bottom left), and EDX maps of 1.4541 exposed to pure ZnNaK//Cl for 800 h at 400 °C.

images, however, a very selective corrosion attack was observed along delta-ferrite phases (**Figure 3**). Interestingly, these phases were corroded severely only when they touched the salt–alloy interfacial surface. Internal delta-ferrite phases were not corroded, as indicated by their lower contrast in BSE mode. This selective corrosion attack is surprising at this low temperature and indicates that the presence of delta-ferrite phases strongly exacerbates corrosion and that alloys containing such phases should not be used as structural materials. After personal communication with experts in the field of high-temperature corrosion (Dechema Research Institute), it became obvious that the 1.4404 steel is susceptible to delta-ferrite formation, as it contains molybdenum and silicon, both ferrite-forming elements.

The cross-sectional BSE images, EPMA element maps, and line scans of 1.4541 under similar conditions are shown in **Figure 4**. The oxide layers are heterogeneous with maximum
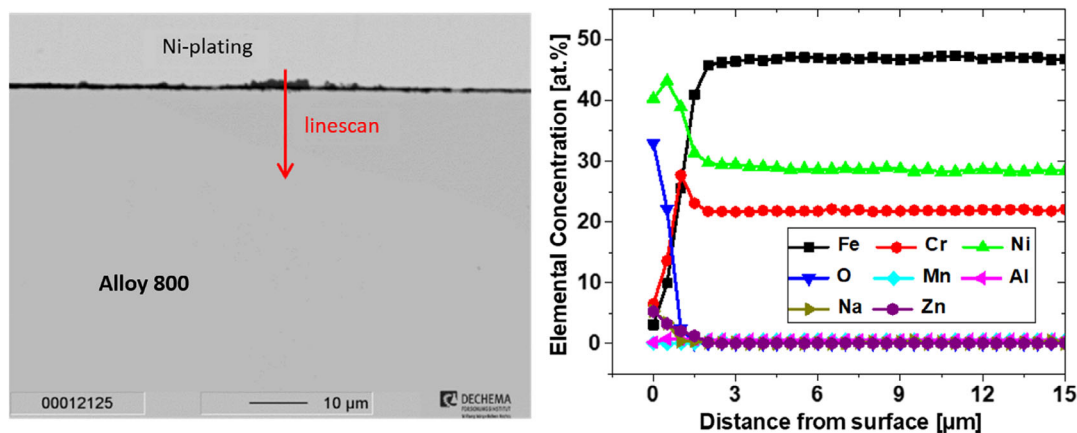

**Figure 4.** BSE image (left) and line scan (right) of 1.4876 exposed to pure ZnNaK//Cl for 800 h at 400 °C.

thicknesses of 4 μm. The oxide layer is enriched in iron and nickel, while chromium is absent. As no Cr-enrichment is observed in the bulk metal, it is possible that chromium was dissolved in the salt matrix and that the Fe–Ni-layer was produced from Cr depletion. This is supported by the fact that the oxide scale is very porous. High concentrations of carbon found throughout the oxide layer show the presence of epoxy resin from the embedding process. Porous oxide scales can basically be formed by two phenomena: by the rapid growth of oxide layers by fast-diffusion and precipitation processes (e.g., growth of magnetite during the corrosion of mild steel P91 in nitrate melts[32]) and by the selective dissolution of one of the elements (e.g., Cr) from the bulk metal into the molten salt. In our case, it is more likely that a selective dissolution process led to a porous oxide scale, as Ni is a slow-diffusing ion and typically the least affected by transport phenomena in molten nitrate and chloride salts (compared to Fe and Cr, see, e.g., a previous study[13]).

3.3. Corrosion in ZnNaK//Cl and Biomass

The influence of the addition of lignin to the molten salt is addressed in this section. The microstructure of 1.4404 after the corrosion experiment is shown in **Figure 5** (top left). The scale thickness is heterogeneous and less adherent (compared to that formed in the pure salt) with a maximum thickness of

≈3 μm. The layered oxide scale consists of an outer Ni and Fe-rich layer, while Cr is still present in the inner layer. Closer to the alloy interface, Ni is enriched and Cr is depleted, but both are attributed to the depletion of iron, rather than an active enrichment.

Given that the oxide scale is rich in carbon, it can be assumed that it is porous and has been infiltrated with epoxy resin during the preparation of the cross section. A Ni-rich layer was formed at the interface to the bulk metal, most likely due to the dissolution of Fe and Cr, but it appears to be nonadhesive and therefore nonprotective. From these results, it can be assumed that the oxide scale is not protective, which is in big contrast to the adherent and dense oxide scale found during exposure to the pure salt. The addition of lignin, conclusively, has a large (negative) impact on the corrosion of 1.4404. Given the complex composition of the biomass feed, it is not possible to break down the corrosion mechanism in detail. Nonetheless, it is reasonable to assume that the biomass, typically simplified as cellulose (see, e.g., a previous study[33]), forms water and CO_2 during decomposition and reacts with the inorganic salts according to the following reactions.

$$ZnCl_2 + H_2O \rightleftharpoons Zn(OH)_2 + 2HCl \qquad (2)$$
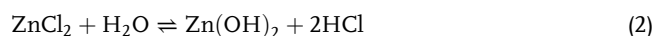
This is a hydrolysis reaction of the chloride salt, which represents reactions with both crystal water and moisture or decomposition products from the biomass. Additionally, the presence
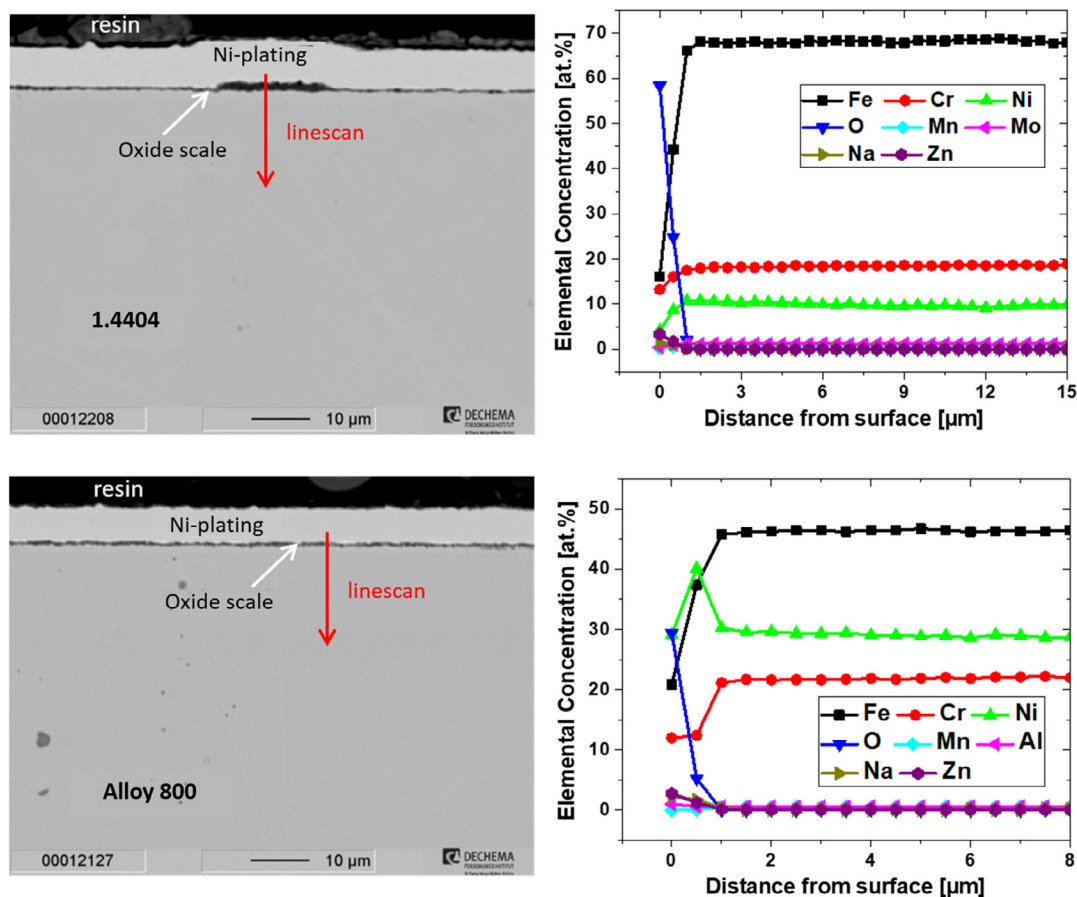

Figure 5. BSE images of 1.4404 (top) and 1.4876 (bottom) and right: the respective line scans. Samples were exposed to ZnNaK//Cl and lignin (1 wt%).
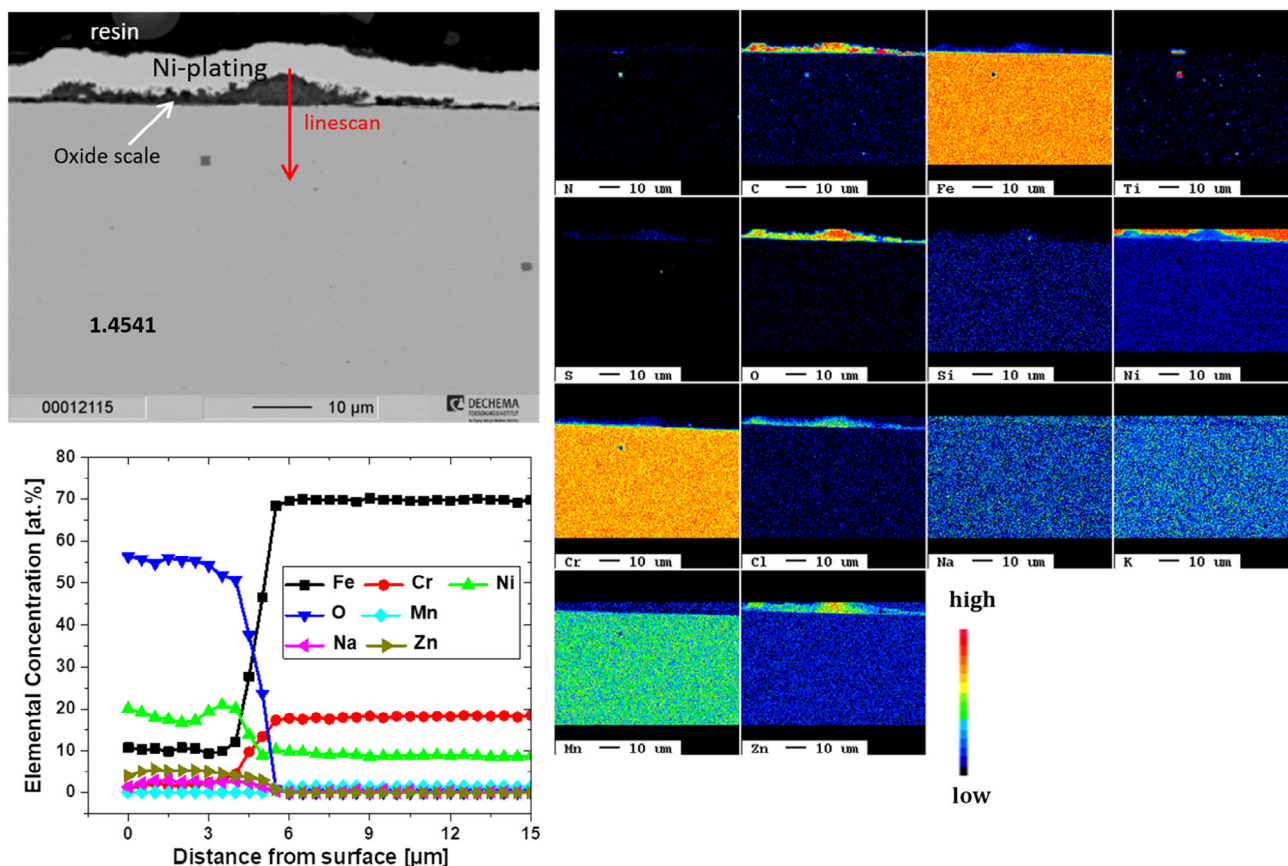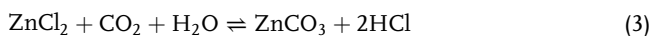
Figure 6. BSE image (top left), line scan (bottom left), and EDX maps of 1.4541 exposed to ZnNaK//Cl and lignin (1 wt%) for 800 h at 400 °C.

of carbon species can lead to the presence of carbon dioxide/monoxide by thermal decomposition of the lignin. Those acidic species can readily react with molten salts to form carbonates, e.g., according to the reaction

$$ZnCl_2 + CO_2 + H_2O \rightleftharpoons ZnCO_3 + 2HCl \tag{3}$$

which is a similar mechanism to that represented in CO_2-capture studies using metal oxides.[34]

The cross-sectional images of 1.4541 are shown in **Figure 6**. The oxide scale thickness varies between 2 and 6 μm and is

thicker, compared to that of 1.4404 (around 1–2 μm from SEM images), and exhibits a morphology similar to that formed in the pure salt. The outer layers are rich in Ni and Fe, indicating that they were formed by the selective dissolution of chromium. The inner layers are enriched in Zn and Na indicating the presence of salt in the corrosion layer. Overall, the formed porous oxide layer (indicated by the epoxy resin present in the pores) can be considered nonprotective. Similar to the oxide scales in the pure salt, the oxide scales of 1.4876 (Alloy 800) exposed to salt + lignin are very thin (<2 μm), adherent, and rich in Ni and O (see the bottom of Figure 5). There appears to be slight
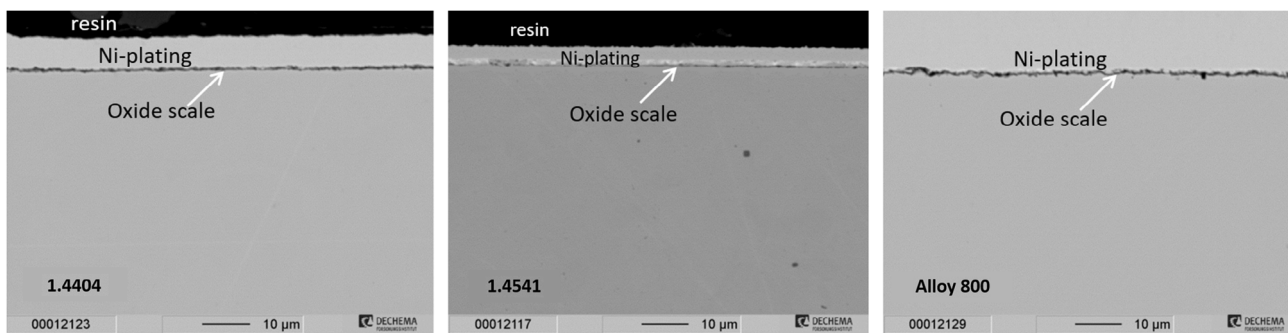

Figure 7. BSE images of 1.4404, 1.4541, and 1.4876 after exposure to ZnNaK//Cl with lignin and ZnO for 800 h at 400 °C.

enrichment of Zn and Na at the interface, but it does not affect the protectiveness of the oxide scale.

3.4. Corrosion in ZnNaK//Cl, Biomass, and ZnO

The third part of the corrosion test included the addition of ZnO, which is supposed to suppress hydrolysis reactions of the molten salt (e.g., analyzed in previous studies[16,17]), thereby reducing its potential corrosivity toward the containment materials. The microstructures of all three alloys exposed to the threefold system are shown in **Figure 7**.

The oxide scales of all three alloys are significantly thinner compared to the pure salt and the salt + lignin experiments. The thicknesses are very similar for all three alloys, 1.4404, 1.4541, and 1.4876, at around 1 μm from SEM images. In all three cases, a dense Ni-rich layer was formed as the only corrosion product, which is in big contrast to the findings from the other test conditions, where Cr depletion and porous oxide scale formation were observed. Depletion of Fe or Cr on neither of the samples can be observed, indicating that the corrosion has stopped after the formation of the Ni-rich oxide layer. Therefore, ZnO addition has successfully reduced the corrosiveness of the salt and assisted in the formation of a denser protective oxide scale.

Based on the experimental results and available literature data, the following assumptions regarding the corrosion mechanism can be made. The pure zinc chloride, containing crystal water, can hydrolyze according to Equation (2), which leads to the formation of corrosive HCl gas. The zinc hydroxide itself will probably dissociate to ZnO, accompanied by the formation of water. The addition of ZnO is likely to reduce the evolution and corrosion reactions of the formed HCl gas. Olsen[16] and later Niazi[17] proposed, respectively, that metal oxides of Ca and Zn can reduce the formation of HCl gas, thereby reducing the corrosive nature of the molten halide salts. In our study, we assume that ZnO captures evolving HCl gas according to the following reaction.

$$ZnO + 2HCl \rightleftharpoons ZnCl_2 + H_2O \uparrow \qquad (4)$$
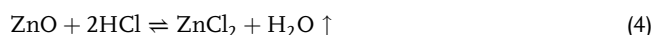
As proposed by Niazi and coworkers, a level of 10 wt% ZnO in ZnNaK//Cl salt reduced the quantity of evolving HCl from >3000 ppmv HCl (in pure salt) to >100 ppmv in the ZnO-doped salt, at 400 °C. The reduced HCl formation and the reduced corrosivity observed in this study strongly suggest that HCl formation is one of the main drivers of corrosion in the ternary ZnNaK//Cl salt. Additional corrosion protection mechanisms may involve a reduction of the molten salt's basicity by the presence of ZnO, which reduces the affinity of the chromium cation to form soluble chromate (see explanations presented regarding Ishitsuka's work[27] in the Introduction section). Overall, these findings demonstrate that molten chlorides containing ZnCl$_2$ can effectively be used for biomass liquefaction even at temperatures exceeding the melting point of ≈200 °C. Corrosion mitigation can be achieved using both simple mixing techniques and cheap chemical reagents, enabling the use of economic construction materials for reactors and other relevant system components.

4. Conclusions

The corrosion of three alloys, 1.4404, 1.4541, and 1.4876, has been investigated in three different conditions: in pure Zn–Na–K//Cl salt (Zn–Na–K: 44.3–13.8–41.9 mol%), a salt–lignin mix (1 wt% lignin), and a salt–lignin–ZnO mix, whereas the ZnO was added as an inhibitor. Alloy 800 was the most stable alloy under all test conditions, forming an adhesive and dense Ni-rich oxide scale, presumably NiO. The scale thickness did not exceed 2 μm, making this alloy the most stable of all three candidate steels. Alloy 1.4404 can also be considered stable in the pure salt, forming a dense adhesive layer, but can contain delta-ferrite phases which are highly susceptible to corrosion. Upon addition of biomass, exacerbated corrosion is observed most likely due to the introduction of oxygen and moisture from the biomass, which accelerates the hydrolysis of the salt and thereby formation of corrosive impurities (e.g., hydroxychlorides and HCl gas). 1.4541 is the least stable alloy and was not found to be corrosion resistant in the pure salt or the salt–lignin mix. Interestingly, the addition of ZnO reduced the corrosivity of the melt substantially, and all three alloys formed dense, protective Ni-rich oxide scales during corrosion. Therefore, it can be concluded that 1.4876 is corrosion resistant under all tested conditions. Molybdenum stabilization in 1.4404 made it per se the second most stable alloy. Yet, the formation of delta-ferrite phases and the inherent selective corrosion make the alloy practically non-usable in the desired application. Alloy 1.4541 should not be used as containment material for the ZnNaK//Cl salt unless substantial amounts of ZnO (>5 wt%) are added to the molten salt.

Conflict of Interest

The authors declare no conflict of interest.

Data Availability Statement

The data that support the findings of this study are available from the corresponding author upon reasonable request.

[1] M. Mehos, H. Price, R. Cable, D. Kearney, B. Kelly, G. J. Kolb, F. Morse, *Concentrating Solar Power Best Practices Study, NREL/TP-5500-75763*, **2020**.

[2] A. Bonk, S. Sau, N. Uranga, M. Herainz, T. Bauer, *Prog. Energy Combust. Sci.* **2018**, *67C*, 69.

[3] D. Brough, H. Jouhara, *Int. J. Thermofluids* **2020**, 1–2.

[4] X. Liu, N. Fechler, M. Antonietti, *Chem. Soc. Rev.* **2013**, *42*, 8237.

[5] V. L. Hammond, L. K. Mudge, *Feasibility study of use of molten salt technology for pyrolysis of solid waste. [Hazardous and municipal wastes], PB-238674/6GA*, **1975**.

[6] H. S. Nygård, E. Olsen, *Int. J. Low-Carbon Technol.* **2012**, *7*, 318.

[7] H. Kawamoto, *J. Wood Sci.* **2017**, *63*, 117.

[8] H. S. Nygård, F. Danielsen, E. Olsen, *Energy Fuels* **2012**, *26*, 6419.

[9] E. Sada, H. Kumazawa, M. Kudsy, *Ind. Eng. Chem. Res.* **2002**, *31*, 612.

[10] S. Czernik, A. V. Bridgwater, *Energy Fuels* **2004**, *18*, 590.

[11] R. H. Venderbosch, W. Prins, *Biofuels, Bioprod. Biorefin.* **2010**, *4*, 178.

[12] W. Ding, A. Bonk, T. Bauer, *Front. Chem. Sci. Eng.* **2018**, *12*, 564.

[13] W. Ding, H. Shi, Y. Xiu, A. Bonk, A. Weisenburger, A. Jianu, T. Bauer, *Sol. Energy Mater. Sol. Cells* **2018**, *184*, 22.

[14] W. Ding, J. Gomez-Vidal, A. Bonk, T. Bauer, *Sol. Energy Mater. Sol. Cells* **2019**, *199*, 8.

[15] W. Ding, H. Shi, A. Jianu, Y. Xiu, A. Bonk, A. Weisenburger, T. Bauer, *Sol. Energy Mater. Sol. Cells* **2019**, *193*, 298.

[16] E. Olsen, M. Hansen, H. S. Nygård, *AIMS Energy* **2017**, *5*, 873.

[17] S. Niazi, E. Olsen, H. S. Nygård, *J. Mol. Liq.* **2020**, *317*, 114069.

[18] A. Kruizenga, *Corrosion mechanisms in chloride and carbonate salts, SAND2012-7594*, **2012**.

[19] S. Guo, J. Zhang, W. Wu, W. Zhou, *Prog. Mater. Sci.* **2018**, *97*, 448.

[20] Y. Li, X. Xu, X. Wang, P. Li, Q. Hao, B. Xiao, *Sol. Energy* **2017**, *152*, 57.

[21] B. Grégoire, C. Oskay, T. M. Meißner, M. C. Galetz, *Sol. Energy Mater. Sol. Cells* **2020**, *216*, 110675.

[22] T. J. Pan, C. L. Zeng, Y. Niu, *Oxid. Met.* **2007**, *67*, 107.

[23] X. Wang, H. Yin, W. Liu, G. Yu, J. He, Z. Tang, L. Yan, *Mater. Corros.* **2019**, *71*.

[24] L. Heikinheimo, D. Baxter, K. Hack, M. Spiegel, M. Hämäläinen, U. Krupp, K. Penttilä, M. Arponen, *Mater. Corros.* **2006**, *57*, 230.

[25] A. Ruh, M. Spiegel, *Mater. Corros.* **2006**, *57*, 237.

[26] M. Sánchez Pastén, M. Spiegel, *Mater. Corros.* **2006**, *57*, 192.

[27] T. Ishitsuka, K. Nose, *Corros. Sci.* **2002**, *44*, 247.

[28] K. Vignarooban, P. Pugazhendhi, C. Tucker, D. Gervasio, A. M. Kannan, *Sol. Energy* **2014**, *103*, 62.

[29] A. Bonk, N. Knoblauch, M. Braun, T. Bauer, M. Schmücker, *Sol. Energy Mater. Sol. Cells* **2020**, *212*, 110578.

[30] J. W. Pugh, J. D. Nisbet, *JOM*, **1950**, *2*, 268.

[31] C. C. Tseng, Y. Shen, S. W. Thompson, M. C. Mataya, G. Krauss, *Metall. Mater. Trans. A* **1994**, *25*, 1147.

[32] A. Bonk, D. Rückle, S. Kaesche, M. Braun, T. Bauer, *Sol. Energy Mater. Sol. Cells* **2019**, *203*, 110162.

[33] A. V. Bridgwater, *Chem. Eng. J.* **2003**, *91*, 87.

[34] B. Deng, Z. Chen, M. Gao, Y. Song, K. Zheng, J. Tang, W. Xiao, X. Mao, D. Wang, *Faraday Discuss.* **2016**, *190*, 241.